Electronic Supplementary Material (ESI) for Chemical Science.

Dispersing Transition Metal Vacancies in Layered Double Hydroxide by Ionic Reductive Complexation Extraction for Efficient Water Oxidation

Yangshan Xie[1], Zheng Wang[1], Min Ju[1], Xia Long[*1], Shihe Yang[*1,2]

1. Guangdong Provincial Key Lab of Nano-Micro Material Research, School of Chemical Biology and Biotechnology, Peking University Shenzhen Graduate School, Shenzhen 518055, China;

2. Department of Chemistry, The Hong Kong University of Science and Technology, Clear Water Bay, Kowloon, Hong Kong, China

Supporting Information

1. Experimental Details S2
2. Results and Discussion S6
3. References S24

Experimental Details

1. Chemicals

Chemicals: Nickel nitrate hexahydrate ($Ni(NO_3)_2•6H_2O$), copper nitrate trihydrate ($Cu(NO_3)_2•3H_2O$), urea ($CO(NH_2)_2$), potassium thiocyanate (KSCN), sodium sulfite (Na_2SO_3), potassium hydroxide (KOH), Iridium oxide (IrO_2), Ruthenium(IV) oxide (RuO_2), ploytetrafluoroethylene preparation (PTFE), absolute ethanol (C_2H_5OH), hydrochloric acid (HCl). Deionized water (18 MΩ) was used to prepare all aqueous solutions. Besides, all chemicals were analytical grade and obtained from commercial suppliers and used without further purification.

2. Synthesis of NiCu LDH

NiCu LDH were synthesized by a hydrothermal method, namely, 1 ml of 10 mM $Ni(NO_3)_2•6H_2O$ aqueous solution and 1 ml of 5 mM $Cu(NO_3)_2•3H_2O$ aqueous solution were mixed in the beaker with 87 ml deionized water. Then 1 ml of 100 mM $CO(NH_2)_2$ was added into the beaker in sequence with magnetic stirring. Nickel foam (about 2 × 3 cm) was carefully cleaned with dilute HCl solution by ultrasonication for 30 min to remove the surface NiO layers, and then sonicated in deionized water and absolute ethanol for 5 min. The above solution and a cleaned piece of nickel foam (2 × 3 cm) were transferred to a 100 ml Teflon lined stainless steel autoclave for hydrothermal reaction at 150 ºC for 48 h, and then allowed to cool to room temperature naturally. Then the NiCu LDH was washed with deionized water/ethanol three times and then dried at room temperature.

3. Fabrication atomic defects on NiCu(I) LDH surface

The NiCu(I) LDH was prepared via an ionic reductive method. Specifically, Na_2SO_3 (1 M) was dissolved in 20 mL of deionized water and stirred to form a clear solution. Then NiCu LDH coated nickel foam was immersed in the above solution with magnetic stirring for 6 days. Then the resulting sample was washed with deionized water/ethanol three times, and dried with a stream of N_2.

4. Fabrication atomic defects on NiCu LDH surface

The NiCu LDH surface with atomic defects was prepared via an ionic reductive complexation extraction (IRCE) method. Specifically, KSCN (1 M) and Na_2SO_3 (1 M) were dissolved in 20 mL of deionized water and stirred to form a clear solution. Then NiCu LDH coated nickel foam was immersed in the above solution with magnetic stirring for various complexation times (3 days, 6 days, 8 days). Then the resulting sample was washed with deionized water/ethanol three times, and dried with a stream of N_2.

5. Materials characterizations

The catalysts were characterized directly by scanning electron microscopy (SEM, ZEISS SUPRA®55) at 5.0 kV and the energy dispersive X-ray Spectroscopy (EDX) analysis were performed on SEM OXFORD X-MAX.

Transmission Electron Microscopy, high resolution TEM (HRTEM) and electron diffraction pattern (ED pattern) were collected on JEM-3200FS. The samples were made by sonication the catalysts off from the nickel foam, then the suspensions with catalyst were dropped onto the copper grid for TEM, ED pattern and HRTEM characterization.

The crystal structure of samples was determined by X-ray diffraction (XRD, D8 Advance X-ray diffractometer) operated at 40 kV and 40 mA with a Cu Kα radiation (λ=1.5405 Å) in the 2θ ranging from 5° to 80° with a step size of 0.02°.

X-ray photoelectron spectroscopy (XPS) spectra were collected on ESCALAB 250XI (ThermoScientific). Spectra were analyzed using XPSPEAK software. The C1s peak for adventitious hydrocarbons at 284.6 eV was used for binding energy calibration.

The concentration of the leached copper ions in complexation solution was quantified by an inductively coupled plasma emission spectroscopy instrument (ICP-AES, JY2000-2).

Zeta potentials of the samples (0.2 mg sample was dissolved in 3 mL of deionized water) were determined by dynamic light scattering analysis (Nano-ZS90) at room temperature.

Electron spin resonance (ESR) measurements were obtained on a Bruker EPR A300 spectrometer. Typically, 5mg sample was placed in a quartz-glass sample tube.

6. Electrochemical performance characterizations

Electrochemical measurements were carried out in a standard three electrode system conducted by a Biological VSP-300 electrochemistry workstation. The as-prepared freestanding catalysts@Ni foam were used as the working electrode, platinum wire and Ag/AgCl electrode were used as the counter and reference electrode, respectively. For IrO_2@Ni foam, 1 mg IrO_2 was dispersed in 0.5 ml ethanol and sonication for 30 min, then 0.5 ml of 4 wt% PTFE was added. After sonication for another 30 min, the catalyst ink was drop dried onto a Ni foam (1 cm × 1 cm). The preparation of RuO_2@Ni foam was the same as that of IrO_2@Ni foam except for using RuO_2 to replace the IrO_2.

The reference was calibrated against and converted to reversible hydrogen electrode (RHE) according to the formula of

$$E\ (vs\ RHE) = E(exp) + E(Ag/AgCl) + 0.059pH$$

All measurements were recorded in 1 M KOH. The cyclic voltammetry (CV) measurements were cycled at a scan rate of 10 mV/s for 20 times until a stable CV curve was achieved before collecting polarization curves and Tafel plots of the catalysts.

Linear sweep voltammetry (LSV) was carried out at 5 mV/s for the polarization curves and 0.5 mV/s for Tafel plots. LSV polarization curves were corrected with 95% iR-compensation.

Chrompotentiometry (CP) was carried out under a constant current density of 10 mA/cm^2, 20 mA/cm^2, and 50 mA/cm^2.

Electrochemical impedance spectroscopy (EIS) analysis were conducted at 1.53 V vs RHE at overpotential of 300mV at DC potential of 5 mV with the frequency ranging from 100 kHz to 0.1 Hz.

The Faradaic efficiency can be calculated as follows[1]:

$$Faradaic\ efficiency = n\ Z\ F/I\ t$$

where n is the number of moles of O_2 evolution, Z is the needed electrons to produce one O_2 molecule, F is the faraday constant (96485 C/mol), t is the time (s), I is the defined current density (A). The electrocatalytic reaction was typically performed at a constant current of 20 mA for 90 min, and 1mL of reactive gas was taken from the reactor with a syringe for analysis using a gas chromatograph (GC-2014C, Lab-solution, TCD, N_2 carrier).

7. Theoretical simulations

All the first-principles spin-polarized calculations were performed using Vienna ab initio simulation package (VASP).[2,3] Projector augmented wave (PAW) potentials were employed to describe the core-valance interactions.[4] And the electronic exchange and correlation was treated by the generalized gradient approximation with the Perdew, Burke, and Ernzerhof (PBE) functional[5] with onsite Hubbard U corrections [6], in which U values for Ni and Cu are chosen as 4.4 and 7.0 eV, respectively, similar to the reported work.[7, 8] The energy cutoff for the plane-wave basis set is set as 400 eV. The convergence criteria is set as 0.001 eV/Å for maximal forces and 10^{-5} eV for energies. Solvation corrections are taken into consideration by relaxing the structures using the implicit solvation model with water as

implemented in VASPsol.[9, 10] The Gibbs free energy ΔG_i (i=1,2,3,4,5) is calculated by $\Delta G_i = \Delta E_i + \Delta ZPE - T\Delta S$ with T set as 298 K. (0001) surface of $NiCu_x$-LDH and SAV-$NiCu_x$-LDH was chosen for the study since it is the most abundant and also the most stable surface. For the SAV-$NiCu_x$-LDH, one cupper atom and one molecule of hydroxide were removed from $NiCu_x$-LDH. The chemical formula of $NiCu_x$-LDH and SAV-$NiCu_x$-LDH is $Ni_7Cu(OH)_{16}CO_3 \cdot (H_2O)_2$ and $Ni_7(OH)_{15}CO_3 \cdot (H_2O)_2$, respectively. All the structures are shown by VESTA.[11]

The mechanism for OER is depicted in Scheme S1, corresponding to the formation of O*, OOH*, OO*, vacant site * and OH*.[12] Here, the free energy difference for every elementary step is given by eq. (S1) to (S5), the maximum value of them determined the overpotential of OER, as indicated by Eq. (S6). By the way, the adsorption free energy of OH* with respect to vacant site * can be obtained by Eq. (S5). We divided the free energy of the catalyst with the bound of OH adsorbate, G(OH*), into three part, the electronic energy of the catalyst with the adsorption of OH species: E(OH*), zero point energy: ZPE and entropy: $T\Delta S$ (Eq. S7), where the latter two terms are not sensitive to different catalysts. E(OH*) can be obtained by summing up the electronic energy of the catalyst without the adhere of OH, the electronic energy of OH and the binding energy of OH to the catalyst, as indicated by Eq. (S9). The same hold true for OOH, given by Eq.(S8) and Eq.(S10). It should be pointed out that we employed a different definition of binding energy of OH* in Eq. S9, in which the energy of OH is directly calculated out, instead of given by the energy difference between water and one half of the energy of hydrogen molecule ($E(H_2O) - 1/2E(H_2)$). According to the definition of E_bOH in Eq. S7, E_bOH is supposed to be a negative value, instead of a positive value, in contrast to the adsorption free energy of OH* defined in Eq. S5, where a positive value was obtained. Combined Eq.S1, Eq.S2, Eq. S7 and Eq.S8, we can derive $\Delta G1+\Delta G2$ as Eq. S11. Since many terms in Eq. S11 remains nearly constant for different catalysts, therefore, they can be regarded as a constant, as defined by Eq. S12. Owning to the linear scaling relationship between E_bOOH and E_bOH, E_bOOH can be conveniently represented by Eq. S13. Here, the coefficient is smaller than one considering the relatively weaker bonding ability of OOH compared to OH. We ultimately obtain Eq. S14, from which we can learn that $\Delta G1+\Delta G2$ mainly relates to the binding energy of OH. A weaker binding energy leads to a smaller value of $\Delta G1+\Delta G2$. Similarly, we can derive $\Delta G1$ as Eq. S15, but cautions should be made here, a weaker binding energy of OH causes an enlarged value of $\Delta G1$ since E_bO is larger than E_bOH ($\lambda > 1$).

$$OH^* \longrightarrow O^* + H^+ + e \qquad \Delta G1$$

$$O^* + H_2O \longrightarrow OOH^* + H^+ + e \qquad \Delta G2$$

$$OOH^* \longrightarrow OO^* + H^+ + e \qquad \Delta G3$$

$$OO^* \longrightarrow * + O_2 \qquad \Delta G4$$

$$* + H_2O \longrightarrow OH^* + H^+ + e \qquad \Delta G5$$

Scheme S1. The general mechanism of oxygen evolution reactions.

$$\Delta G1 = G(O^*) + 0.5 * G(H_2) - G(OH^*) \qquad \text{Eq. S1}$$

$$\Delta G2 = G(OOH^*) + 0.5 * G(H_2) - G(O^*) - G(H_2O) \qquad \text{Eq. S2}$$

$$\Delta G3 = G(OO^*) + 0.5 * G(H_2) - G(OOH^*) \qquad \text{Eq. S3}$$

$$\Delta G4 = G(OO^*) - G(^*) - G(O_2)$$ Eq. S4

$$\Delta G5 = G(OH^*) + 0.5^* G(H_2) - G(^*) - G(H_2O)$$ Eq. S5

$$\eta = \frac{\max\{\Delta G1, \Delta G2, \Delta G3, \Delta G4, \Delta G5\}}{e} - 1.23$$ Eq. S6

$$G(OH^*) = E(OH^*) + ZPE(OH^*) - T\Delta S(OH^*)$$ Eq. S6

$$G(OOH^*) = E(OOH^*) + ZPE(OOH^*) - T\Delta S(OOH^*)$$ Eq. S7

$$E(OH^*) = E(OH) + E(^*) + E_bOH$$ Eq. S8

$$E(OOH^*) = E(OOH) + E(^*) + E_bOOH$$ Eq. S9

$$\Delta G1 + \Delta G2 = E_bOOH - E_bOH + E(OOH) - E(OH) + ZPE(OOH^*) - ZPE(OH^*) - T\Delta S(OOH^*) + T\Delta S(OH^*) - G(H_2O) + G(H_2)$$ Eq. S10

$$C1 = E(OOH) - E(OH) + ZPE(OOH^*) - ZPE(OH^*) - T\Delta S(OOH^*) + T\Delta S(OH^*) - G(H_2O) + G(H_2)$$ Eq. S11

$$E_bOOH = \xi \times E_bOH \quad (0 < \xi < 1)$$ Eq. S12

$$\Delta G1 + \Delta G2 = (\xi - 1)\ E_b\mathrm{OH} + C1 \quad (0 < \xi < 1, E_bOH < 0, C1 > 0)$$ Eq. S13

$$\Delta G1 = (\lambda - 1)\ E_bOH + C2 \quad (1 < \lambda, E_bOH < 0, C2 > 0)$$ Eq. S14

Results and Discussion

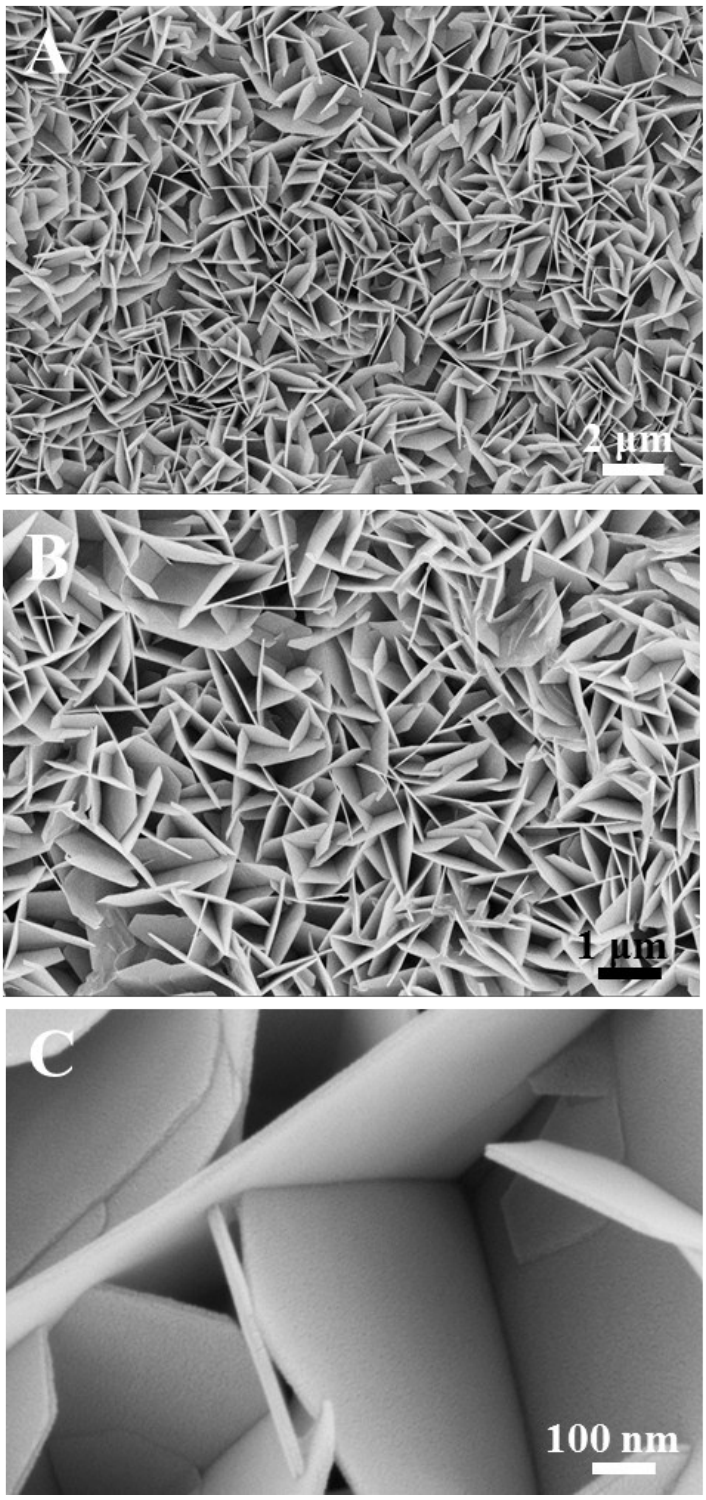

Fig. S1. SEM images of NiCu LDH in different magnifications.

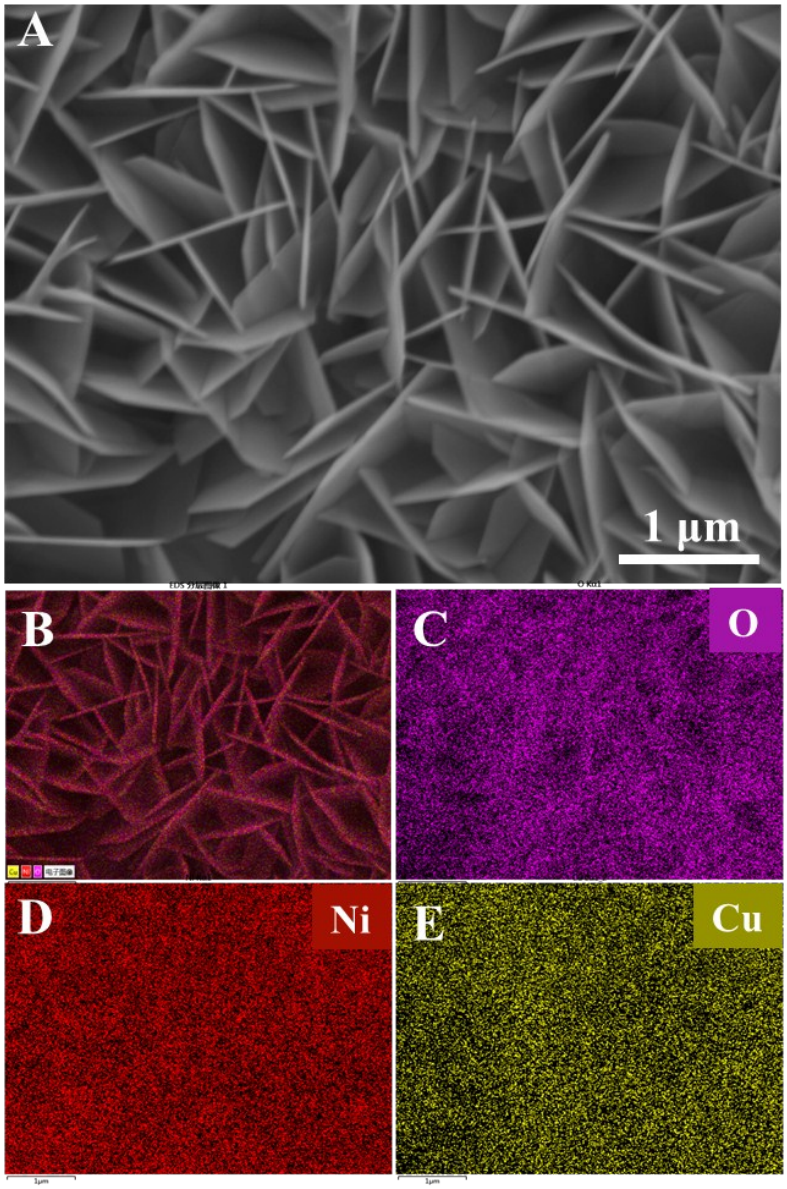

Fig. S2. SEM and the corresponding elemental mapping images of NiCu LDH. (A) SEM image, (B) the combined elemental, (C) O, (D) Ni, and (E) Cu mapping.

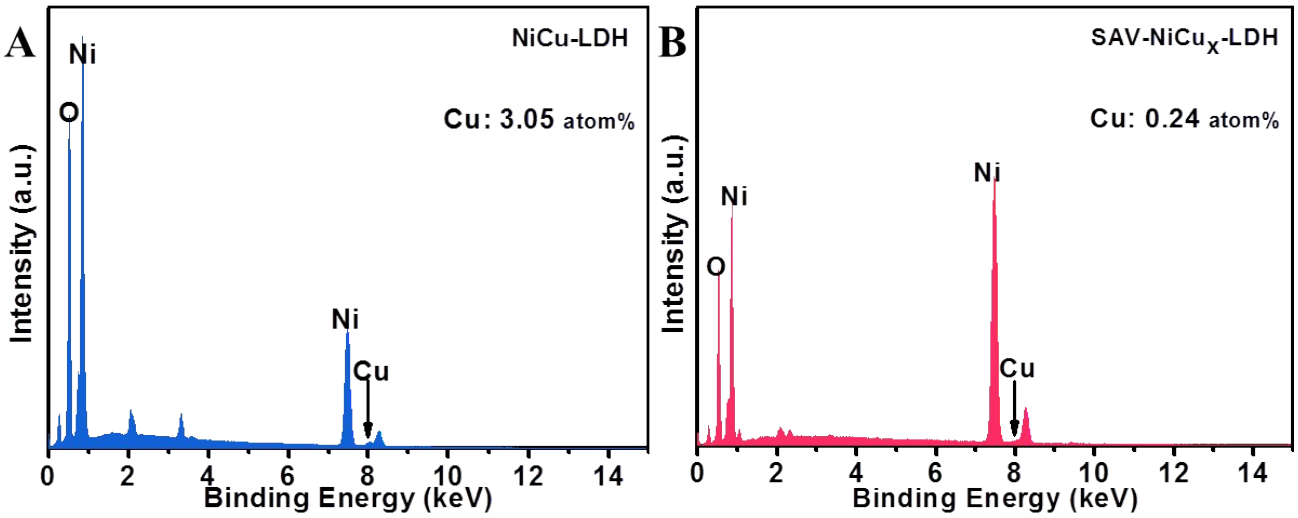

Fig. S3. The EDX patterns of (A) NiCu LDH and (B) SAV-NiCu$_x$ LDH.

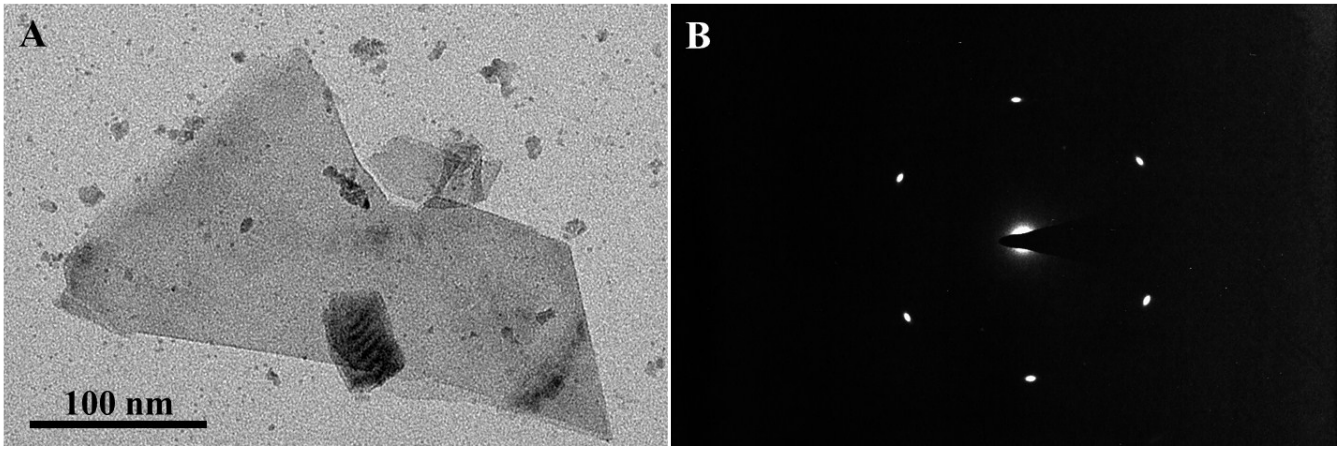

Fig. S4. TEM image (A) and the corresponding electron pattern (B) of NiCu LDH.

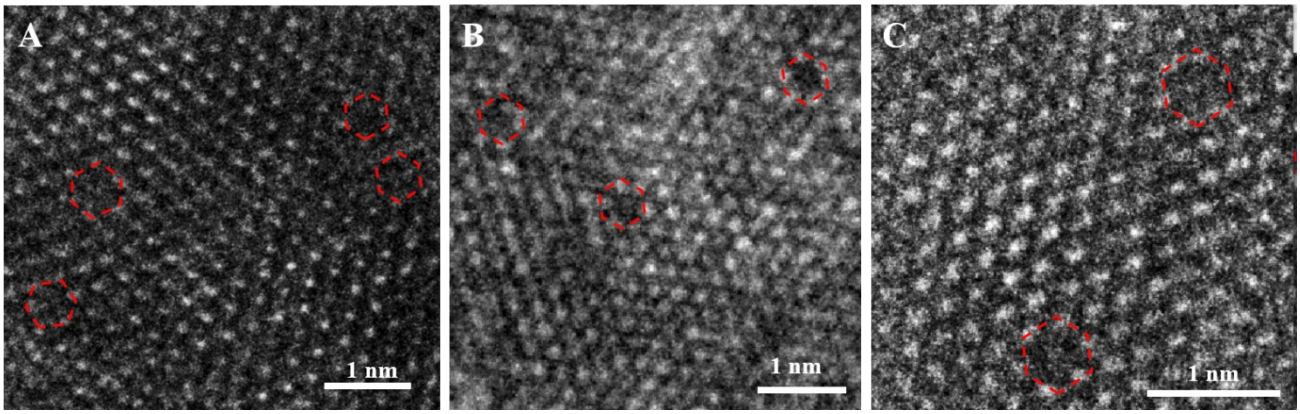

Fig. S5. More HRTEM images of the SAV-NiCu$_x$ LDH showing the atomic vacancies.

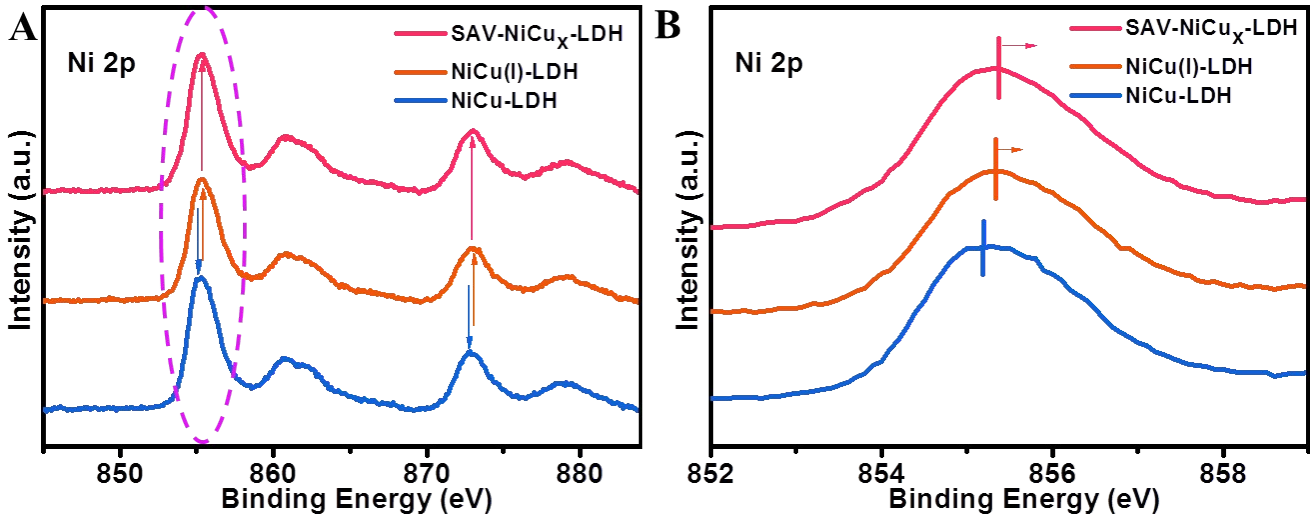

Fig. S6. High resolution XPS spectra of NiCu LDH (blue curve), NiCu(I) LDH (orange curve) and SAV-NiCu$_x$ LDH (red curve) in the Ni 2p spin-orbital.

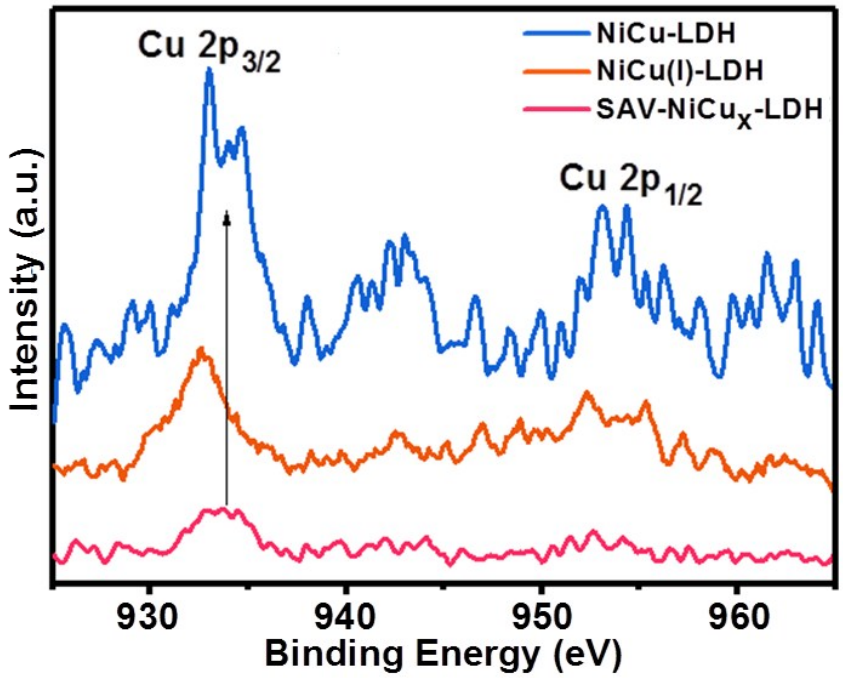

Fig. S7. High resolution XPS spectra of NiCu LDH (blue curve), NiCu(I) LDH (orange curve) and SAV-$NiCu_x$ LDH (red curve) in the Cu 2p spin-orbital.

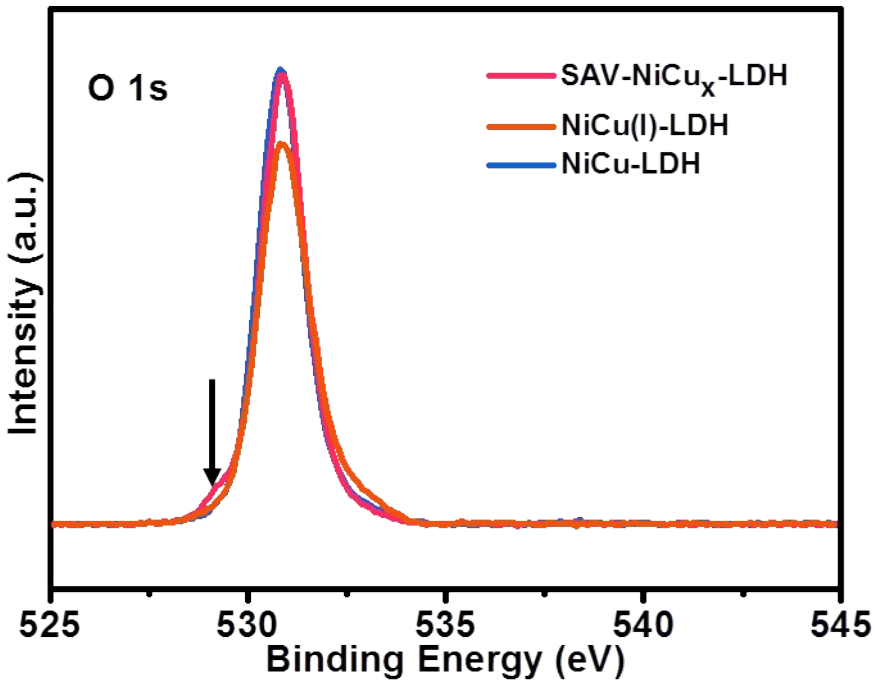

Fig. S8. High resolution XPS spectra of NiCu LDH (blue curve), NiCu(I) LDH (orange curve) and SAV-$NiCu_x$ LDH (red curve) in the O 1s spin-orbital.

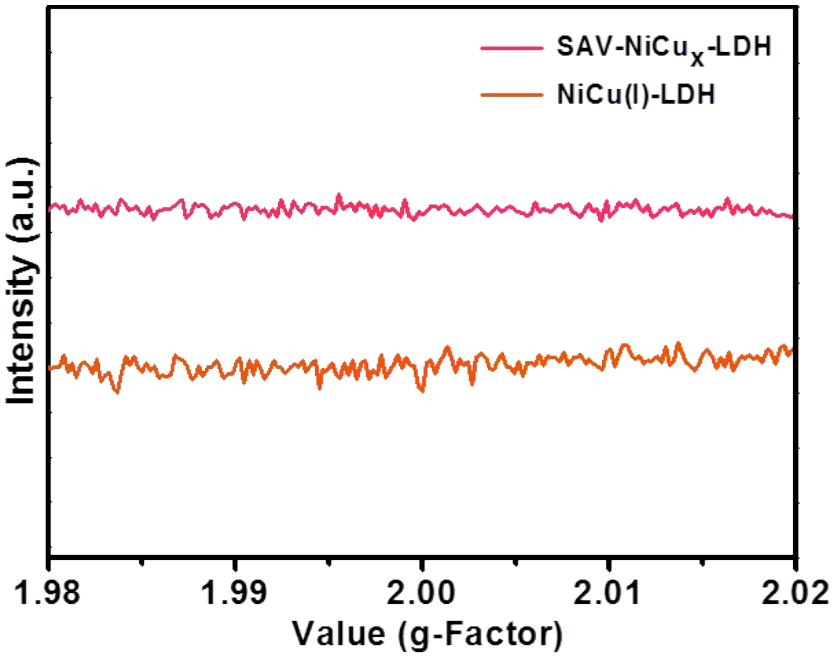

Fig. S9. EPR spectra of NiCu(I) LDH (orange curve) and SAV-NiCu$_x$ LDH (red curve).

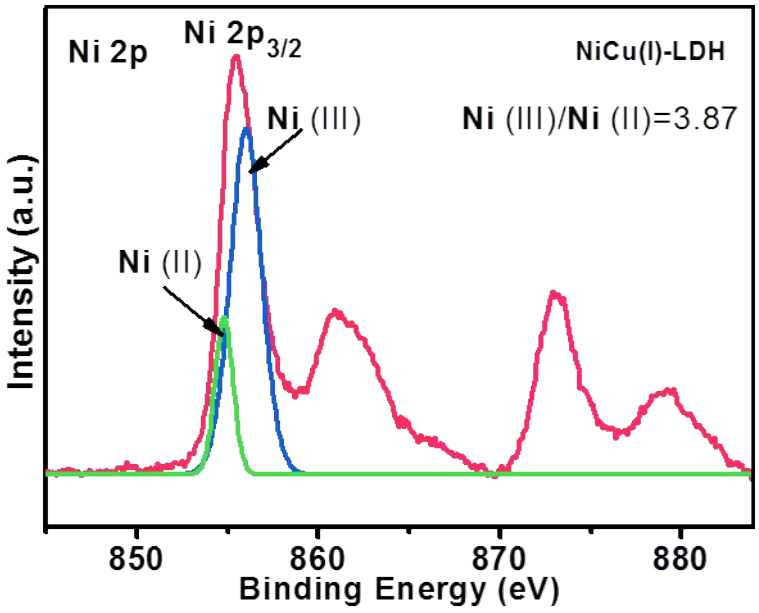

Fig. S10. Deconvoluted XPS spectra of Ni 2P spin-orbitals in NiCu(I) LDH.

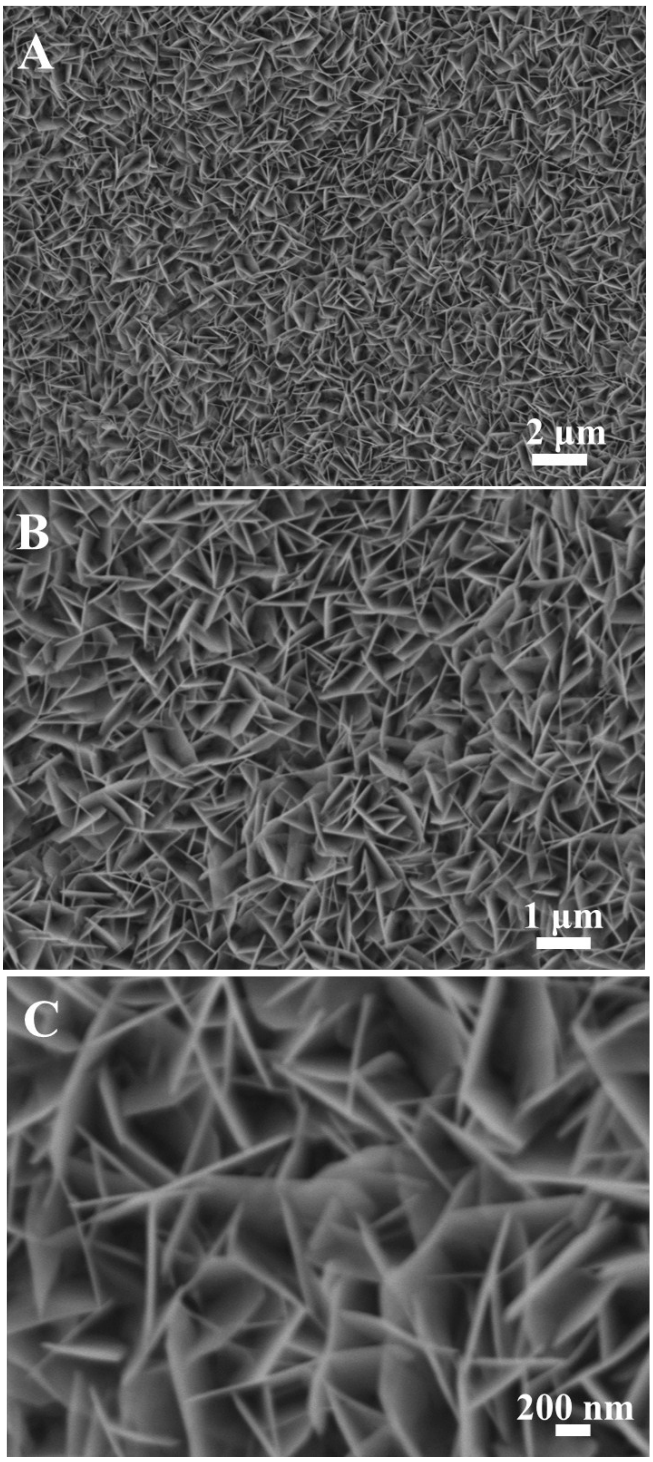

Fig. S11. SEM images of NiCu(I) LDH under different magnifications.

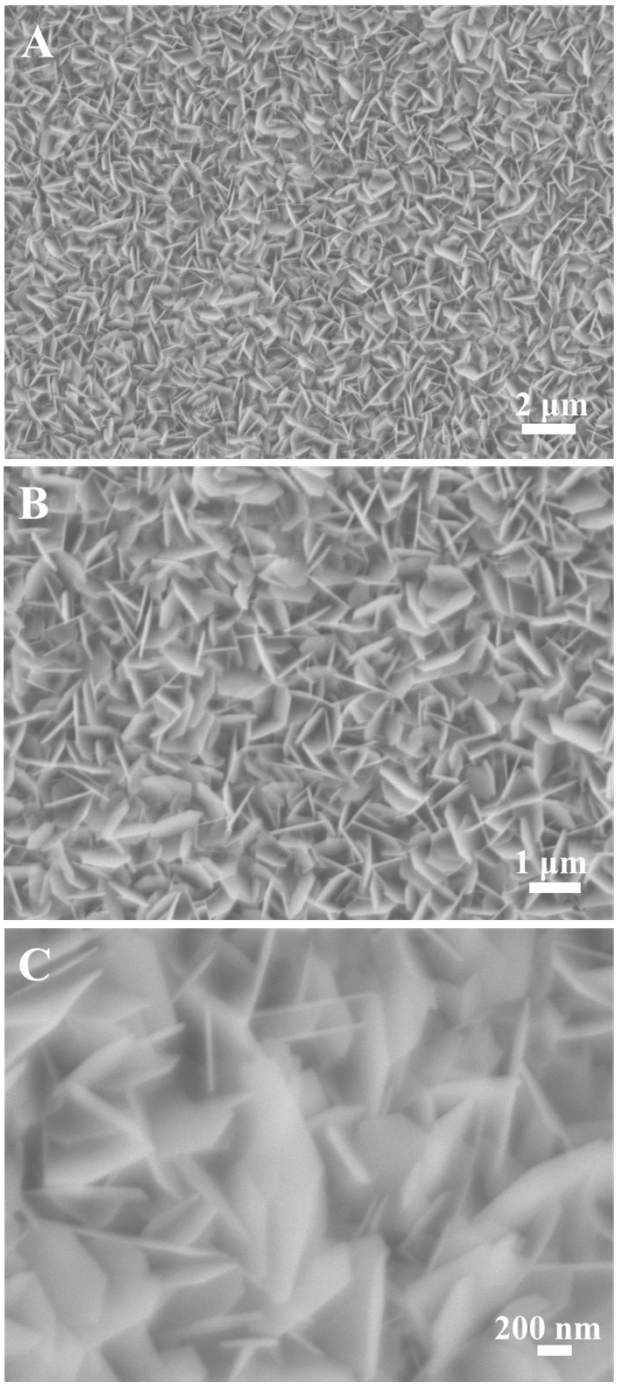

Fig. S12. SEM images of $Ni(OH)_2$ under different magnifications.

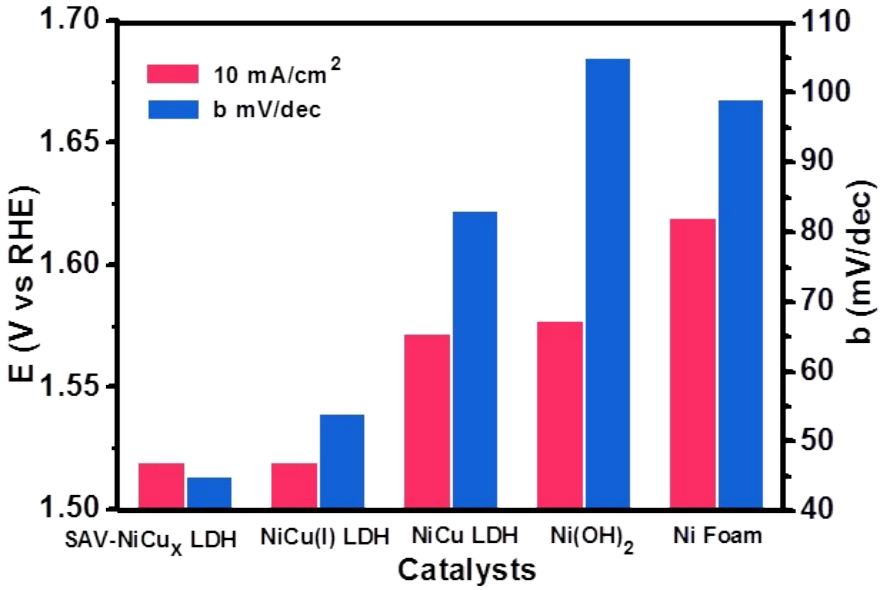

Fig. S13. Bar chart of the potential at the current density of 10 mA/cm^2 (red) and Tafel slope (blue) of the as-prepared catalysts and control catalyst.

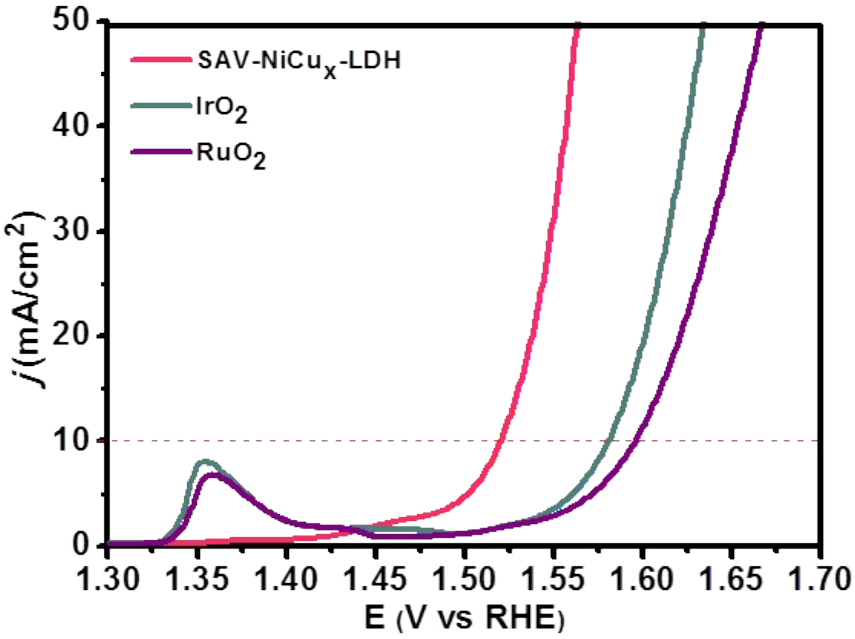

Fig. S14. LSV curves of SAV-NiCu$_x$ LDH (red curve), IrO$_2$ (green curve) and RuO$_2$ (purple curve).

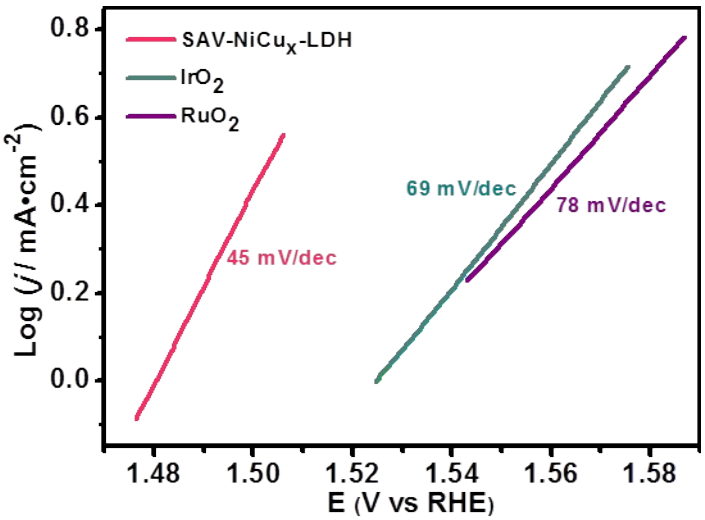

Fig. S15. Tafel plots of SAV-NiCu$_x$ LDH (red curve), IrO$_2$ (green curve) and RuO$_2$ (purple curve).

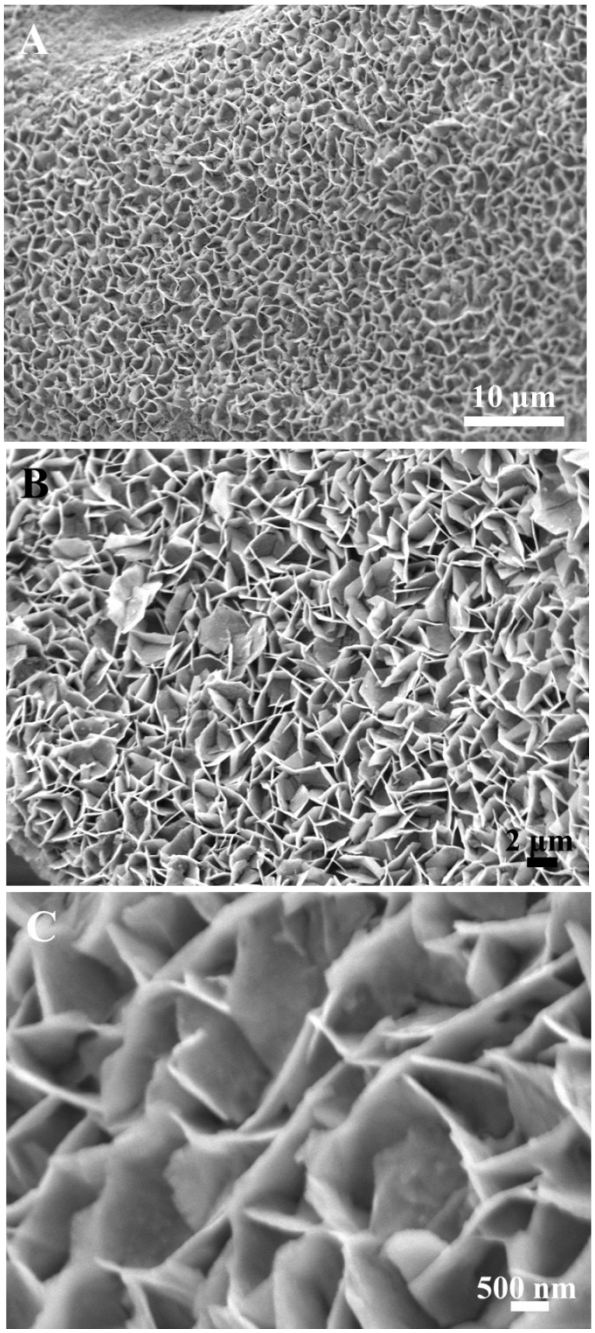

Fig. S16. SEM images of SAV-NiCu$_x$ LDH after the long-term stability tests.

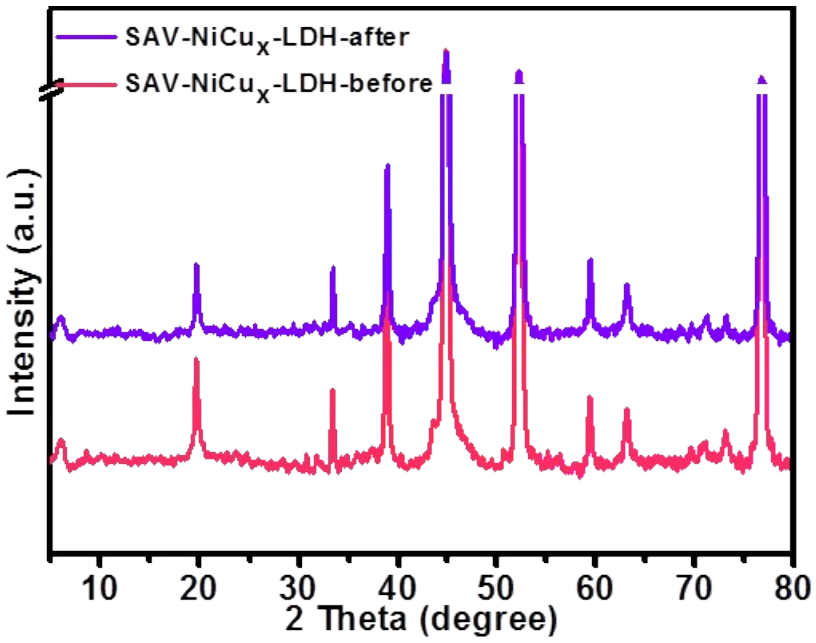

Fig. S17. XRD patterns of SAV-NiCu$_x$ LDH before (red curve) and after (purple curve) the long-term stability tests.

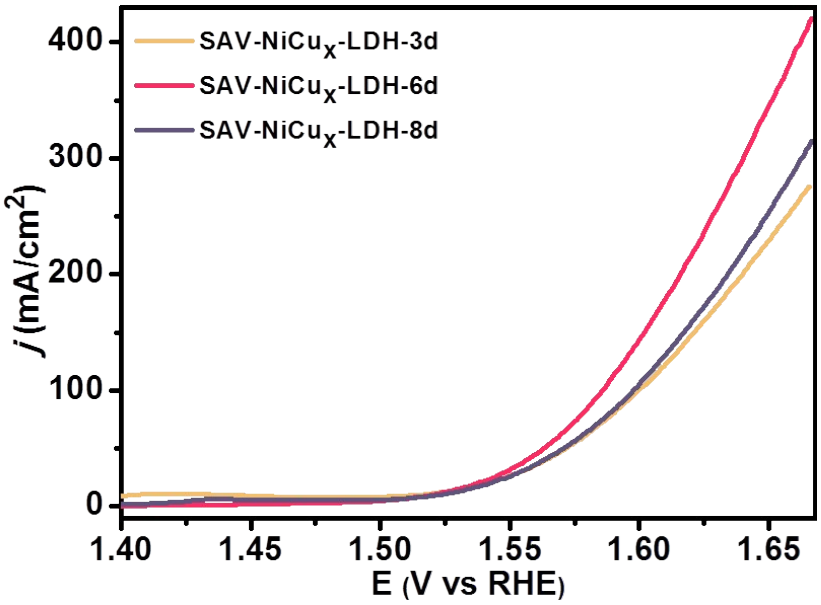

Fig. S18. LSV curves of SAV-NiCu$_x$ LDH after complexation treatment for different times (yellow, red and violet curves for 3d, 6d, and 8d).

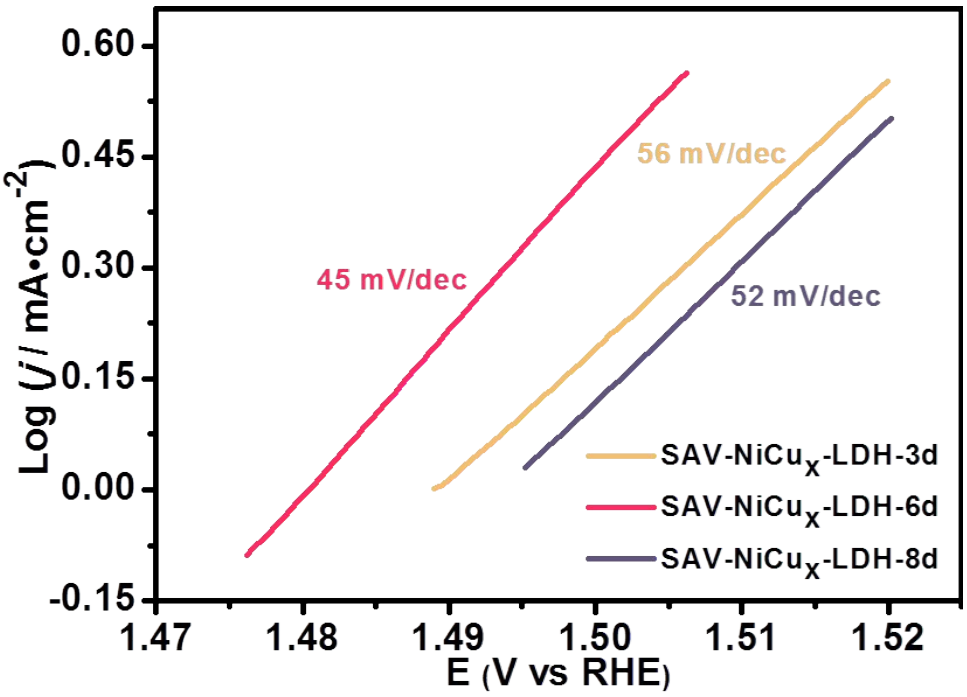

Fig. S19. Tafel slopes of SAV-$NiCu_x$ LDH after complexation treatment for different times (yellow, red and violet curves for 3d, 6d, and 8d).

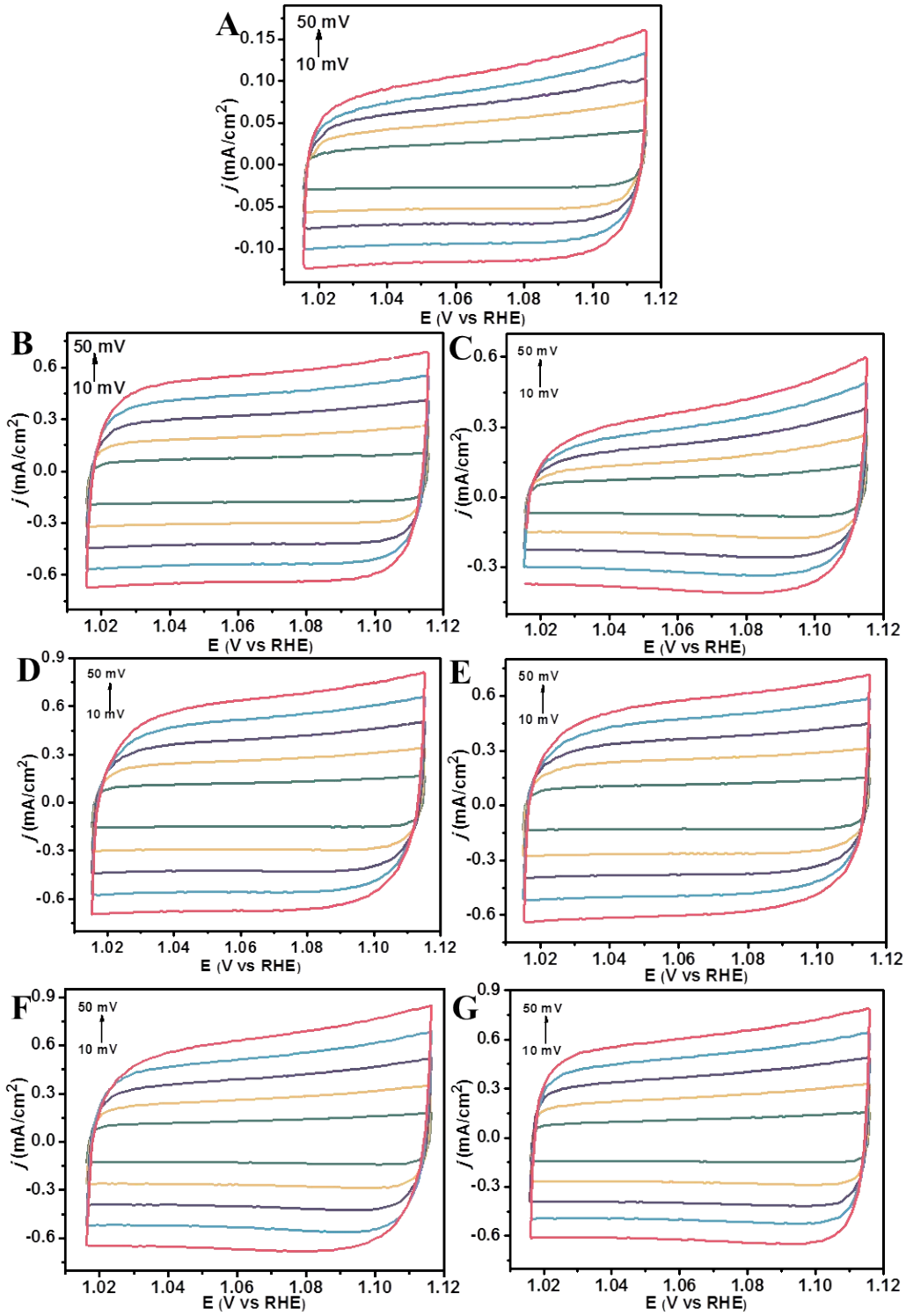

Fig. S20. CV curves collected at different scan rates. (A) Ni foam, (B) $Ni(OH)_2$, (C) NiCu LDH, (D) NiCu(I) LDH and SAV-$NiCu_x$ LDH obtained by different complexation time (E, F and G curves for 3d, 6d, and 8d).

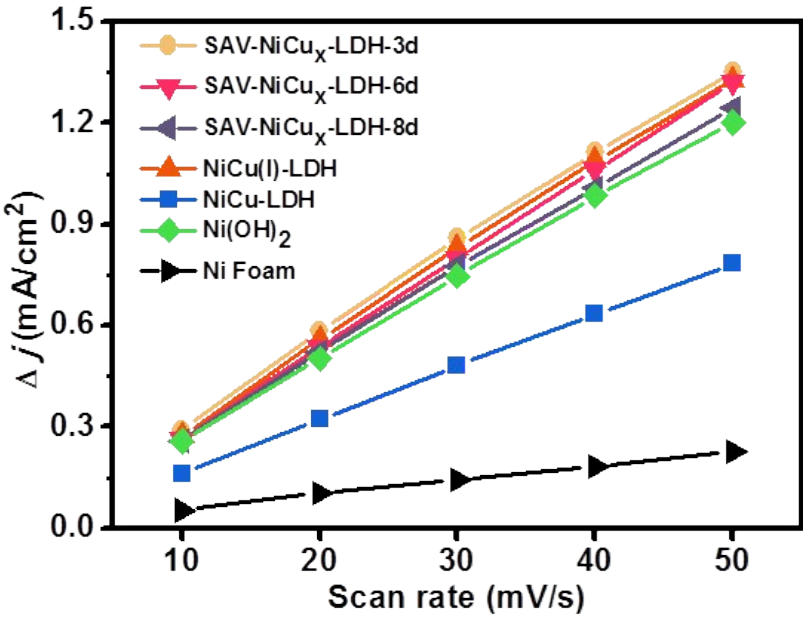

Fig. S21. The Δ*j* as the function of scan rates for Ni foam (black curve), $Ni(OH)_2$ (green curve), NiCu LDH (blue curve), NiCu(I) LDH (orange curve) and SAV-$NiCu_x$ LDH obtained by different complexation time (yellow, red and violet curves for 3d, 6d, and 8d).

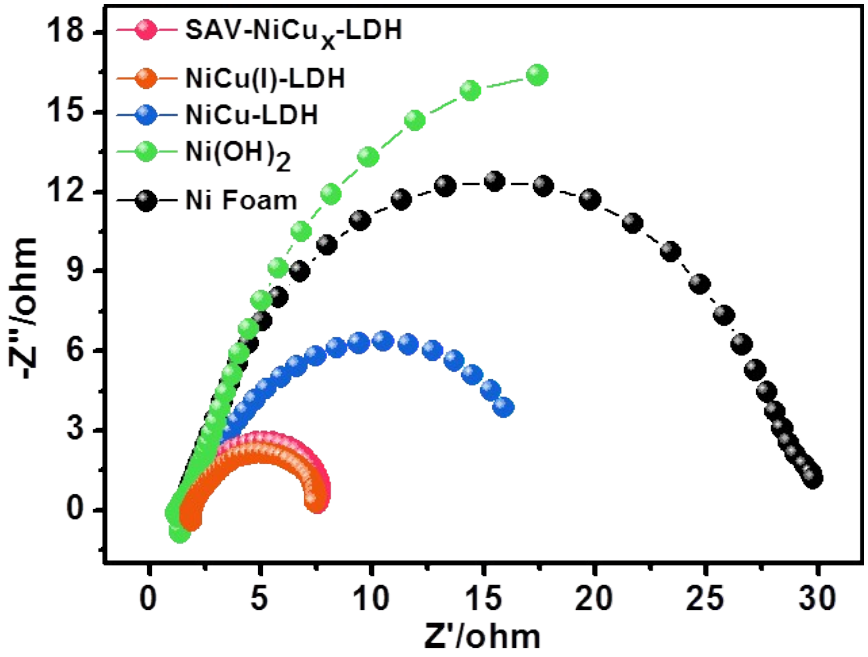

Fig. S22. Nyquist plots of Ni foam (black curve), $Ni(OH)_2$ (green curve), NiCu LDH (blue curve), NiCu(I) LDH (orange curve) and SAV-$NiCu_x$ LDH (red curve).

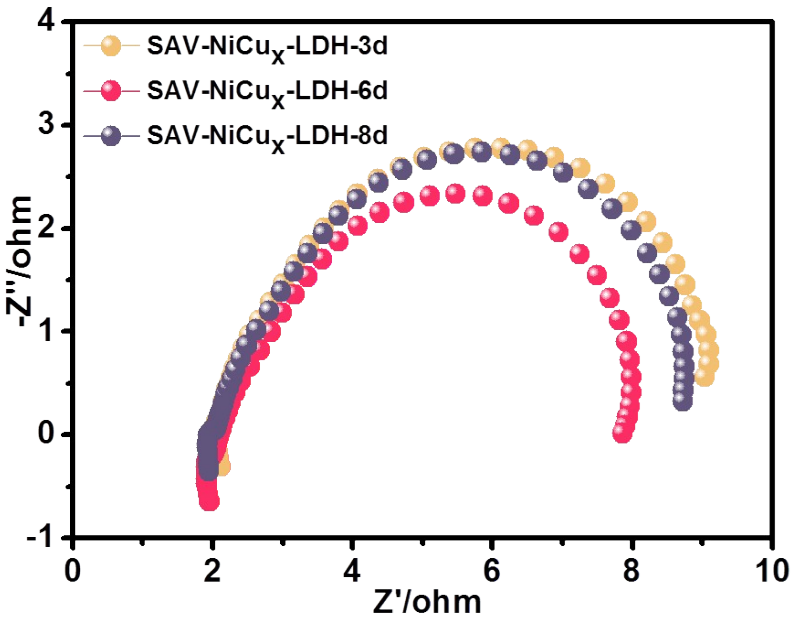

Fig. S23. EIS spectra of SAV-NiCu$_x$ LDH obtained after various complexation time (yellow, red and violet curves for 3d, 6d, and 8d).

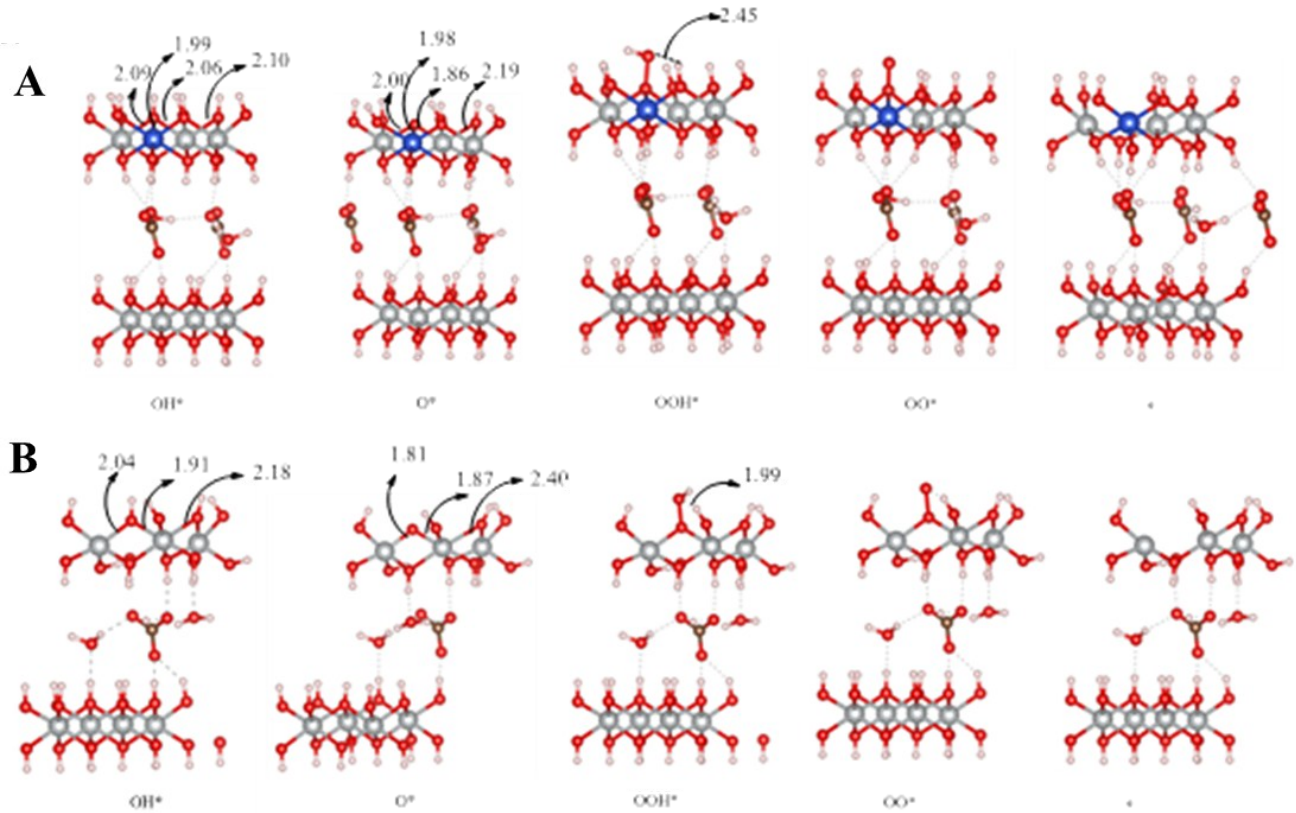

Fig. S24. The structures of key intermediate: OH*, O*, OOH*, OO* and * for (A) NiCu-LDH and (B) SAV-NiCu$_x$-LDH. Selected bond lengths are given in Å (gray balls represent Ni, bule balls represent Cu, red balls represent O and white balls represent H, respectively.).

Table S1. The XPS data of NiCu LDH, NiCu(I) LDH and SAV-$NiCu_x$ LDH showing the concentrations of elements.

Elements	Atom %		
	NiCu LDH	NiCu(I) LDH	SAV-$NiCu_x$ LDH
Ni 2p	23.49	23.38	21.51
O 1s	50.01	55.39	53.87
Cu 2p	1.84	1.31	0.01

Table S2. The fitting data of Ni element in SAV-$NiCu_x$ LDH

	SAV-$NiCu_x$ LDH							
	Peak 1	Peak 2	Peak 3	Peak 4	Peak 5	Peak 6	Peak 7	Ni(III)/Ni(II)
Width	1.17254	2.38293	3.51496	3.21692	1.99673	1.60336	4.04051	2.03
Height	7646.166	16254.24	8617.125	1405.397	9653.406	1977.472	4427.509	2.13
Area	11236.48	48544.35	37961.41	5666.29	24157.95	3973.757	22421.03	4.32

Note: peak 1 and peak 2 represent Ni(II) and Ni(III), respectively.

Table S3. The fitting data of Ni element in NiCu LDH

	NiCu-LDH							
	Peak 1	Peak 2	Peak 3	Peak 4	Peak 5	Peak 6	Peak 7	Ni(III)/Ni(II)
Width	1.25573	2.20063	3.73163	2.84263	1.83164	1.80469	3.65883	1.75
Height	10151.47	14082.53	7939.974	1187.124	8898.669	2426.377	4084.063	1.39
Area	15976.66	38840.75	37134.55	4229.379	20428.02	5488.073	18728.15	2.43

Note: peak 1 and peak 2 represent Ni(II) and Ni(III), respectively.

Table S4. The C_{dl} calculation results of Ni foam, $Ni(OH)_2$, NiCu LDH, NiCu(I) LDH and SAV-$NiCu_x$ LDH obtained by different complexation time (3d, 6d, and 8d).

Samples	Slope	C_{dl} (μF)
Ni foam	0.00423	2.12
$Ni(OH)_2$	0.0237	11.85
NiCu LDH	0.0156	7.80
NiCu(I) LDH	0.02642	13.21
SAV-$NiCu_x$ LDH-3d	0.02649	13.25
SAV-$NiCu_x$ LDH-6d	0.0264	13.20
SAV-$NiCu_x$ LDH-8d	0.02458	12.29

Table S5. The calculated standard free energy of OER of NiCu LDH and SAV-$NiCu_x$ LDH.

Intermediate	NiCu LDH	SAV-$NiCu_x$ LDH
OH*	0	0
O*	1.51	1.50
OOH*	3.47	3.26
OO*	3.85	3.96
*	3.48	3.24

References

1 F. Song and X. Hu, *Nat. Commun.*, 2014, **5**, 4477.
2 G. Kresse and J. Furthmüller, *Comp. Mater. Sci.*, 1996, **6**, 15-50.
3 G. Kresse and J. Furthmüller, *Phys. Rev. B* 1996, **54**, 11169-11186.
4 P. E. Blöchl, *Phys. Rev. B*, 1994, **50**, 17953-17979.
5 J. P. Perdew, K. Burke and M. Ernzerhof, *Phys. Rev. Lett.*, 1996, **77**, 3865-3868.
6 V. I. Anisimov, Berlin, Heidelberg, 1995.
7 A. J. Tkalych, J. M. P. Martirez and E. A. Carter, *Phys. Chem. Chem. Phys.*, 2018, **20**, 19525-19531.
8 M. Nolan and S. D. Elliott, *Phys. Chem. Chem. Phys.*, 2006, **8**, 5350-5358.
9 K. Mathew, R. Sundararaman, K. Letchworth-Weaver, T. A. Arias and R. G. Hennig, *The Journal of Chemical Physics*, 2014, **140**, 084106.
10 K. M. a. R. G. Hennig, *arXiv* 2016, 1601.03346.
11 K. Momma and F. Izumi, *J. Appl. Crystallography*, 2011, **44**, 1272-1276.
12 J. Rossmeisl, A. Logadottir and J. K. Nørskov, *Chem. Phys.*, 2005, **319**, 178-184.